https://doi.org/10.5194/gi-2024-14
Preprint. Discussion started: 9 December 2024

Geoscientific Instrumentation Methods and Data Systems Discussions

The Harwell TCCON observatory

Damien Weidmann[1], Richard Brownsword[1], and Stamatia Doniki[1]

[1]STFC Rutherford Appleton Laboratory, Space Science and Technology Department, Harwell Campus, Didcot, Oxfordshire, OX11 0QX, UK

Correspondence: Damien Weidmann (damien.weidmann@stfc.ac.uk)

Abstract. The Harwell observatory, located in Oxfordshire, UK, now part of the Total Carbon Column Observatory Network (TCCON), has been performing ground-based remote sensing of averaged dry columns of atmospheric greenhouses since September 2020. Measurements are performed through near infrared and short wave infrared high-resolution spectroscopy of the atmosphere's transmission in solar occultation viewing mode, following the TCCON methodology. We report on the development, the measurements, and the performance of the observing system installed at Harwell. The hardware and software are described and characterized, as well as the outputted data quality, based on the four year data record collected so far. The Harwell site is demonstrated to produce data of high quality, well in line with the requirements for the TCCON infrastructure.

1 Introduction

The Total Carbon Column Observatory Network (TCCON) is an essential international, coordinated, collaborative ground-based infrastructure providing measurements of the column-averaged dry volume mixing ratio (VMR) of atmospheric water vapour and deuterated water vapour (H_2O and HDO), carbon dioxide (CO_2), methane (CH_4), nitrous oxide (N_2O), carbon monoxide (CO), and hydrogen fluoride (HF). The measurements are carried out using high-resolution ground-based Fourier transform spectroscopy of the atmosphere in the zenith solar occultation viewing mode.

The network started in 2004 and has grown to currently 30 nationally-supported observing stations across the Earth, supporting global greenhouse gas (GHG) measurements and associated sciences. TCCON has become essential for satellite data product calibration and validation, and is operationally used for missions such as NASA OCO2 (Wunch et al., 2017), ESA SENTINEL 5P (Sha et al., 2021), JAXA GOSAT (Taylor et al., 2022), CNSA TanSat (Yang et al., 2020), and for forth-coming ones such as EUTMETSAT CO2M and CNES MicroCarb, to name only a few. The TCCON data are also used for carbon cycle studies (Messerschmidt et al., 2013) and regional emission estimation, either as stand alone dataset (Babenhauserheide et al., 2020; Mottungan et al., 2024) or together with satellite data (Byrne et al., 2024). In addition, TCCON forms a reference framework to anchor denser and/or more localized networks (for instance national GHG observation networks) made of smaller instruments (Frey et al., 2019; Sha et al., 2020), and can be used to maintain traceability through a network of networks characterizing GHG emissions at finer scales.

The establishment of a site in the UK for ground-based remote sensing of greenhouse gases (GHG) started in 2015. The objective was to set up the full observing system in compliance to the Total Carbon Column Observatory Network requirements and seek the network accreditation (Brownsword et al., 2021), in adherence to the TCCON charter and methodology to include

https://doi.org/10.5194/gi-2024-14
Preprint. Discussion started: 9 December 2024

Geoscientific Instrumentation Methods and Data Systems Discussions

new site in the network. This paper describes the implementation of the UK observatory, so-called the Harwell TCCON site and its hardware and software components, and provides evidences of compliance against the TCCON instrumental and data quality requirements, and describes the current status of the dataset now covering nearly four years.

Due to the development of new buildings at the Harwell campus compromising the TCCON observatory field of view, the site was moved by 50 metres about one year after starting operation. Therefore this paper also provides a re-characterization for the Harwell site at its new location since the previous accreditation report (Brownsword et al., 2021).

2 Location and setting

The Harwell TCCON installation is sited at the Rutherford Appleton Laboratory, some 6 km SW of the town of Didcot in Oxfordshire. The site has coordinates 51.571°N, 1.315°W and lies 141 m above the mean sea level (AMSL) on the southern perimeter of the Harwell Campus with a southerly view over predominantly arable farmland. Figure 1 shows the general location within the British Isles, and the local settings.

The diurnal wind rose from the Harwell site meteorological station recorded between 14/09/2022 and 14/09/2023 is shown in an inset of Figure 1. The retained data for the wind rose corresponds to the observational conditions: no rain, wind speed below 7 m/s, and at least 100 W/m^2 of solar flux. The prevailing winds are westerlies and south-westerlies. Considering the global airmasses affecting the UK weather (UK Met Office, 2018), these corresponds to the returning polar maritime and the tropical maritime airmasses. The Harwell site is therefore well situated to obtain data on the large scale atmospheric exchanges between the Atlantic and continental Europe. Local sources of greenhouse gases are primarily related to agricultural activities, and some medium size urban centres. The closest town, Didcot, has a natural gas 1.4 GW power station that is a major local source of CO_2. However, the plant is located 6.5 km from the Harwell site on a bearing of 30°; the chance of transport to the Harwell site is less than 5% according to the 2022 wind rose. Besides, the site is located upwind of London when considering the prevailing winds, which is of interest for characterization of GHG emissions of the greater London area.

https://doi.org/10.5194/gi-2024-14
Preprint. Discussion started: 9 December 2024

Geoscientific Instrumentation Methods and Data Systems Discussions

Figure 1. Harwell TCCON setting. Left, general site location within the UK. The insert in the bottom left gives the diurnal yearly wind rose for the site (2022-2023). Right, Close-up of the Harwell scientific campus indicating the mostly rural surroundings, apart for the small town of Didcot in the north-west. Background images ©Google Earth.

3 Instrumental system description

The description of the measurement system implemented at the Harwell site, and its verification described in the following sections, is underpinned and framed by the TCCON measurement system requirements. These are recalled in Table 1.

Table 1. Summary of the main instrumental requirements for a TCCON measurement system. The acronyms in the table stand for OPD: optical path difference, ZPD: zero path difference, SNR: signal to noise ratio, ME: modulation efficiency, TBC: to be confirmed, TBI: to be implemented.

Requirement	Range or limit	Status	Requirement	Range or limit	Status
Spectral range	< 4000 - 9000 cm^{-1}	Pass	Spectral resolution	< 0.02 cm^{-1}	Pass
OPD	≥ 45 cm	Pass	O_2 band SNR	≥ 200	Pass
Phase resolution	≥ 1 cm^{-1}	Pass	CO_2 1.60 µm band SNR	≥ 700	Pass
Sun pointing error	<0.8 mrad	Pass	CO_2 2.06 µm band SNR	≥ 700	Pass
Surface pressure error	<0.3 mbar	Pass	Acquisition time	150 s	Pass
Surface temperature error	< 1 K	Pass	Detector coupling	DC	Pass
ZPD crossing time error	<1 s	Pass	Lineshape monitoring	In beam	Pass
Laser sampling error	<1.4×10^{-4} step	Pass	Lineshape analysis	LINEFIT	Pass
Monthly HCl spectrum SNR	>2500	Pass	Level 2 retrieval	GFIT	Pass
ME variation over OPD	<5%	Pass	In situ measurements	p, T	Pass
Phase error	±10 mrad TBC	Pass	Independent validation	EM27 travelling std	TBI

https://doi.org/10.5194/gi-2024-14
Preprint. Discussion started: 9 December 2024

Geoscientific Instrumentation Methods and Data Systems Discussions

3.1 Spectrometer

The spectrometer is a Bruker Fourier Transform Spectrometer (FTS) model IFS120/5 HR (S/N GI003092). The maximum optical path difference (OPD) is 6 m leading to a maximum resolution of 0.0015 cm^{-1} (per Bruker definition of resolution, which is $0.9/OPD$). A top view of the FTS with covers removed is shown in Figure 2, in which an illustration of the optical path has been overlaid. At the bottom right is the source compartment. A flip mirror allows to select the radiation to be injected into the interferometer: either an internal source or external radiation entering on the side of the source compartment, so that it forms an image onto the input FTS aperture. The latter input is used for TCCON measurements. The input radiation must be at $f/6.5$ and enters with an angle of ~7°to the normal to the input window.

The exit aperture of the beamsplitter compartment is re-imaged at the centre of the sample compartment, in which the detectors have been installed. The beam is recollimated and split into two components by a dichroic filter transmitting > 0.9 from 3700 to 11200 cm^{-1} and reflecting > 0.9 between 625 to 825 nm. The high-frequency reflected part is focused onto a Si detector (area 1.2 mm^2) by a 2-inch diameter and 2-inch focal length off-axis paraboloid mirror (OAPM). Before the focusing, an anti-aliasing filter (Thorlabs FGL665) is added into the beam (low-pass, 3dB cut-off frequency of ~15900 cm^{-1}). Given the space constraint, the filter had to be inserted in the collimated part of the beam. It has been checked not to produce any significant fringing to the infrared/visible transmission spectra. The low frequency part is transmitted to be focused in the same manner onto a InGaAs detector (area 1 mm^2). In the figure, the detectors can be seen as installed in the upper sample compartment. The optical arrangement has retained the option to use the other sample compartment (lower one in fig. 2) together with a range a different detectors from the detector compartment.

The FTS is equipped with the dual acquisition electronics allowing simultaneous acquisition of the InGaAs and the Si detector signals. Outputs of the respective detectors pass successively through a pre-amplifier, a low-pass filter (LPF) and a main amplifier. For solar measurements, unit gain is applied in all cases and the cut-off frequency of the LPF is matched to the velocity of the scanning mirror. For HCl calibration spectra, using a tungsten lamp source, the detectors are operated in AC mode to increase the dynamic range and the InGaAs detector operated at an increased gain of 10.

The FTS is not operated under vacuum nor under inert atmosphere.

3.2 Sun tracking

A high precision alt-azimuth (Robinson et al., 2020) solar tracker was developed in-house to capture the radiation input to be directed into the FTS. A rotation stage with a large central aperture of 120 mm diameter was used to control the pointing azimuth angle of the tracker. Its unidirectional angular repeatability is given to be 5 μrad (PI PRS200 6449921111). The large aperture of the azimuth stage ensures that the distance between the tracker and the solar input coupling optics (517 mm effective focal length) can be as long as 12.9 m. The elevation angle of the tracker is controlled by another high-precision rotation stage with a 2 μrad repeatability (PI L-611.9ASD). Azimuth and elevation plane mirrors are identical, made of 20 mm thick aluminium ellipses of dimension 184 mm × 130 mm. The mirrors are nickel and gold plated with a surface quality better than $\lambda/5$ at 633 nm.

https://doi.org/10.5194/gi-2024-14
Preprint. Discussion started: 9 December 2024

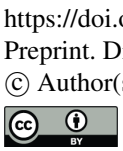

Geoscientific Instrumentation Methods and Data Systems Discussions
Open Access
EGU

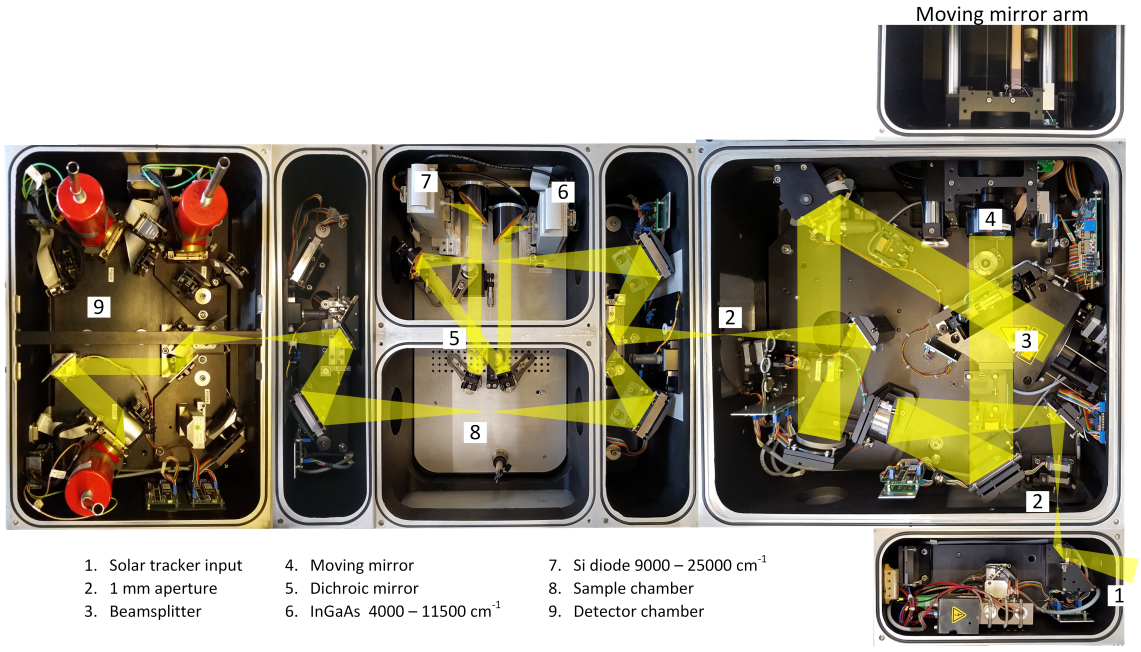

Figure 2. Top view of the opened Fourier Transform Spectrometer (FTS) with a representation of the optical path overlaid.

To limit environmental exposure, the azimuth stage and the mirror assembly are housed in Delrin compartments, kept white to limit radiative heating. For structural strength, the elevation stage is enclosed in an aluminium compartment, protected by a pressed-steel radiation shield. Temperature of the stages is actively monitored: when the temperature exceeds 30° C a forced convection cooling is activated, and over 40° C the system is switched off as beyond the operational range of the stages, to avoid damage. Resistive heating pads are activated when necessary to maintain the stage temperature above 10° C. The whole system is installed in a motorized clam-shell dome, installed on the roof of our laboratory within the Harwell Campus as shown in Fig.3. The distance between the first mirror of the tracker and the input aperture of the FTS is 9.5 m.

Together with the sun pointing hardware, a dedicated feedback system was developed using the camera tracking approach (Gisi et al., 2011), and programmed with LabVIEW. A HD CMOS camera (1280 ×1024) equipped with a 20 mm focal length bi-convex lens is inserted into the source compartment of the FTS to produce an image of the interferometer input aperture plane with a magnification of 0.25. Because of the volume taken by the input selection switching mirror assembly within the spectrometer, the camera system could only be inserted at a 15°angle with respect to the normal of the input aperture plane. The camera is aligned so that its central pixel corresponds to the centre of the FTS input aperture image. A picture from the feedback camera in false color taken by the CMOS camera during operation is shown in the central part of Fig.4.

Within the LabVIEW control software, once all the conditions are fulfilled to start solar occultation measurements, the tracker points to the theoretical apparent location of the sun given the time and the geolocation. The SUNAE algorithm is used for the calculations (Walraven, 1978; Michalsky, 1988), implemented in LabVIEW. Due to the imperfect alignment of the

https://doi.org/10.5194/gi-2024-14
Preprint. Discussion started: 9 December 2024

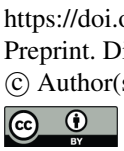

Geoscientific Instrumentation Methods and Data Systems Discussions

Figure 3. Left, view of the alt-azimuth high pointing precision solar tracker operating in the astronomical dome. Right, general view of the roof installation within the Harwell Campus (Drone image courtesy of Melina Zempila).

tracker, the solar disc may not be within the 2.2°×2.8°field of view of the tracking camera when the system goes on. In this case, a database of offset corrections generated from historical data is used. Once the Sun is within the image, the NI Vision library is used to recognize the vector between the position of the solar disk centre and that of the FTS central aperture. Motion correction signals to the alt-azimuth stages are then sent for recentering. The pointing update rate is 1 Hz. The transfer function between the alt-azimuth angles and the camera image reference frame axis requires a three point sensitivity calibration. This is measured by purposely generating a known change in azimuth and elevation angles while the Sun is centred, and determining the corresponding pixel vector change observed for the Sun's centre in the camera image. Sensitivity and offset calibration needs repeating only if the optical alignment of the solar radiation delivery arm is altered.

3.3 Calibration cell input

By default the spectrometer input is the solar scene. By manually changing a plane and an off-axis paraboloid (OAP) mirrors using pre-aligned magnetic posts, it can be switched to the calibration cell input. The cell is filled with pure HCl (Hase et al., 2013). For the calibration arm, the light source is a tungsten halogen bulb (Osram, 50 W, 12 V, 900 lumen) collimated with a 25 mm diameter, 40 mm focal length CaF_2 lens. A spherical confocal reflector behind the lamp also collects some radiation. The collimated light is directed through the HCl calibration cell (100 mm long, 25 mm diameter, ~5 mbar pressure) and then focused into the spectrometer using an OAP (F/7, focal length 17.8 cm) to form an image on the FTS input aperture wheel. The calibration cell currently used for this external calibration, carried out monthly, was provided by the TCCON community and calibrated with the parameters listed in Table 2, cell ID 49. Residual cell impurities such as air and water vapour require the use of effective cell parameters for network-wide consistency of lineshape monitoring, to avoid the need to provide separate partial pressures for all constituents. The effective pressure is the pressure of pure HCl that would give the observed linewidths in the presence of impurities (Hase et al., 2013).

https://doi.org/10.5194/gi-2024-14
Preprint. Discussion started: 9 December 2024

Geoscientific Instrumentation Methods and Data Systems Discussions

In June 2021, the HCl calibration cell was inserted in the solar beam to provide an additional real time quality metric during operation. A duplicate cell was recently acquired for redundancy, whose properties are also given in Table 2.

Table 2. Description of the two calibration HCl gas cells used for Harwell site calibration.

Cell ID	49	#10 (2022)
Origin	KIT, DE	Caltech, USA
Calibration date	Nov. 2015	Aug. 2022
Spectroscopic Database	HITRAN 2008	HITRAN 2020
Effective pressure $H^{35}Cl$ @ 296 K	4.865 hPa	5.0489 hPa
Effective pressure $H^{37}Cl$ @ 296 K	4.963 hPa	-
$H^{35}Cl$ column retrieved	$1.3479 \cdot 10^{22} molec/m^2$	$1.2346 \cdot 10^{22} molec/m^2$
$H^{37}Cl$ column retrieved	$1.3427 \cdot 10^{22} molec/m^2$	-

3.4 Meteorological station

The meteorological station is composed of 1) an anemometer and a rain gauge (Gill Instruments Maximet GMX240), a sun pyranometer (Gill Instruments Maximet GMX101), and 3) a pressure (p), temperature (T), and relative humidity (RH) sensor (Vaisala PTU-307). The p, T, RH sensor is calibrated every year to maintain accuracies of ±0.20 hPa at 20°C, ±0.2 °at 20°C, and ±1% for a 0-90% RH range. A duplicate p, T, RH sensor system, re-calibrated by the manufacturer and swapped annually, allows continuous logging of data to TCCON accuracy standards.

All meteorological data are time-stamped, acquired with a 1 Hz rate, smoothed, and logged every minute using the TCCON observatory Labview control software.

3.5 Timing

To ensure accurate time-stamping of the acquired spectra, the TimeTools T100 Network Time Protocol server was used to synchronise the control PC of the FTS, with an accuracy of 3 ms. The spectra acquired receive their timestamp from the internal FTS controller, which, via the Opus software, is synchronized from the control PC of the FTS running Opus (Kivi and Heikkinen, 2016; Heikkinen and Kivi, 2020). On the control PC, the Bruker Opus software was set to update its time reference from the PC clock every hour. The GPS antenna connected to the TimeTools server was installed on the pole holding the meteorological instruments referred to above.

The timestamps of the spectra as contained in the Opus format files, are then used to calculate the zero path difference (ZPD) timestamp as described in (Toon, 2009). Early on, an anomaly was found in the way interferogram peak locations are

https://doi.org/10.5194/gi-2024-14
Preprint. Discussion started: 9 December 2024


Geoscientific Instrumentation Methods and Data Systems Discussions
Open Access
EGU

stored in the data output from the Opus software, specifically associated with the FTS firmware version 2.485. The solution was implemented as part of the processing chain and is described in Section 5.

3.6 Observation automation

To benefit from the increased data throughput brought by observation automation (Geddes et al., 2018; Geibel et al., 2010), a purpose-built LabVIEW software was developed. It controls all the subsystems required for conducting measurements (dome, sun tracker, meteorological station, spectrometer) as well as the overall measurement schedule and its automation.

The automation software is divided into a set of independent applications that communicate with each other over TCP connections. They can even be distributed across separate computers. Figure 4 shows the graphical user interface of some of the applications.

The "weather station" application collects data from the meteorological measurement hardware, and also the temperature from the sun tracker rotation stages. From the data collected, it determines whether the dome needs opening or closing. The following conditions are required to trigger dome opening:

- Sun elevation must be above 10°.
- Sun flux must be above a previously recorded threshold during clear sky conditions, given the solar elevation angle.
- Rainfall must be 0 mm.
- Wind velocity must be below 6 m/s.

The "All sky dome" application controls dome operations, based on inputs from the "weather station" one, or from manual operation if the "weather station" application is not running. To avoid short sunny spells, frequent in the South East of England, activating frequent opening/closing sequences, the opening conditions must be fulfilled for at least 5 min to trigger the actual opening. Similarly, the dome closes if any of the observation conditions is not fulfilled for a continuous period of 5 min. If rain is detected by a sensor integrated into the dome by the manufacturer, however, closure is immediate.

The "RAL tracker" application controls the Sun tracker hardware, the associated camera, and calculates the tracking feedback. It communicates with the "All sky dome" application, as Sun tracking is obviously dependent of the dome status, and with the "FTS control" application that needs to know if spectra acquisition is required.

The "FTS control" application communicates with the "RAL Tracker" one, and with the OPUS software installed on the FTS control computer. OPUS does not support TCP communication and imposes instead the fairly old DDE (Dynamic Data Exchange) communication standard.

All the applications mentioned communicates with the "Log viewer" one, that provides a user interface to look at log files and events created by the individual applications organized as a searchable database.

During operation, all the files (Opus files, Meteorological data file, automation log files) are written locally on the FTS control PC. The Task Scheduler of the Windows OS was used to automate the daily transfer of the local files to a backed up archive. Every day at 23:55 local time, the files of the day are transferred, ready for processing.

https://doi.org/10.5194/gi-2024-14
Preprint. Discussion started: 9 December 2024

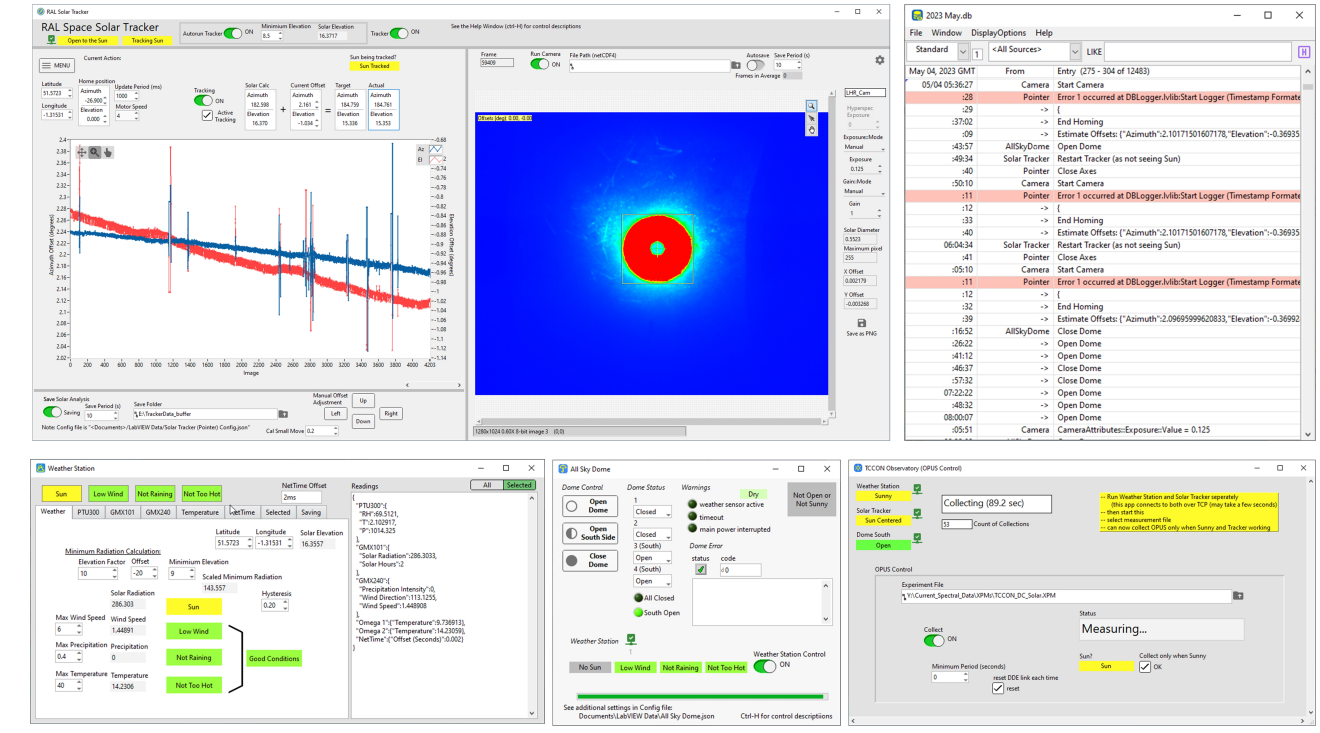

Figure 4. Composite picture of the Graphical User Interfaces of the five independent Labview applications underpinning the Harwell site automated operation. From top left clockwise, solar pointing, camera control, log database of operation events, OPUS FTS control interface, dome operation, and weather station control. The camera image shows the video of the FTS input aperture plane. In the Figure the saturated image of the sun disc co-aligned to the 1 mm input aperture can be seen.

4 System performance

The performance of the instrumental system is evaluated against the requirements set by the TCCON community (Wunch et al., 2011) summarised in Table 1. Some requirements relate to the settings of the FTS and are not detailed any further. In this section the focus is on the instrument performance characterization.

4.1 Signal to noise ratio

When measuring transmission spectra of the atmosphere, the signal to noise ratio (SNR) achieved for the short wave infrared region (InGaAs detector channel) is maintained between 300 and 600, depending on atmospheric conditions and elevation angles. The input optical signal is attenuated to avoid detector saturation that may trigger interferogram non-linearity. Some examples of estimates, from the residuals of the transmittance spectral fittings, can be seen in Section 5. From these particular residuals, the SNR is 463 (417) for the CO_2 window centred at 6340 cm^{-1} (CH_4 window centred at 6002 cm^{-1}). The sun

https://doi.org/10.5194/gi-2024-14
Preprint. Discussion started: 9 December 2024


Geoscientific Instrumentation Methods and Data Systems Discussions

elevation was 27°, about half of the maximum one achievable at the Harwell location in the summer. The infrared region (Si detector channel) provides SNR of about 250 for the measurement of the O_2 A-band (760 nm).

The expected SNR from the instrument can be estimated, using, for instance, the simplified expression from (Treffers, 1977) for a rapid scanning interferometer. In the case of TCCON solar occultation measurements, which use a bright source, we consider the photon shot noise as dominating. The corresponding noise equivalent power (NEP) for purely Poissonian unpolarized light is expressed by Eq. 1, with P_ν the spectral flux *detected* by the detector (includes quantum efficiency). Calculating the expected SNR, given the InGaAs and Si detector spectral responses gives 700 and 900 respectively. This is within the order of magnitude of what is observed, given the simplicity of the SNR model.

$$NEP_{ph}^2 = 2\int h\nu P_\nu d\nu \tag{1}$$

When the calibration measurements are made with the external source, 200 repetitions of the standard single-sided forward-backward acquisition are averaged to produce a spectrum with an SNR of 3000. Acquisition time is approximately 8 hours.

4.2 Instrument calibration

The instrument performance is monitored each month by measuring and analysing a high SNR transmission spectrum of the HCl calibration cell (ID: 49), as described in (Hase et al., 1999). The LINEFIT analysis software is used to infer the instrument lineshape (ILS) from the experimental HCl spectral lines, as any lineshape uncertainty will contribute to error on the retrieved gas column VMR (Hase et al., 2013).

The simple parametrization of the ILS model was used when running LINEFIT. The spectral window of analysis was selected to be 5670-5805 cm^{-1}. The results of more than 3 years of monthly ILS measurements are summarized in Fig. 5. The spectrometer is consistently well within the requirement of $<5\%$ of modulation efficiency (ME) variation over the OPD, as the ME plot in Fig. 5 only shows the extrema picked up from each of the ME vs OPD output analysis. The repeated column value for $H^{35}Cl$ shows a systematic bias of 0.7% and a one sigma scatter of 0.4%. The residual between the LINEFIT-inferred ILS and the modelled one used in the retrieval processor shows small discrepancies. In the near future, we will look into using the measured lineshape as input parameter for column retrieval.

4.3 Sun pointing

The RAL Sun tracker precision was assessed by using the record of the actual azimuth and elevation angles as reported during a tracking event. To extract the short-term random error element, azimuth and elevation records are subtracted from the calculated theoretical Sun pointing. The residual offsets (differences between actual and calculated angular positions) are further de-trended from slowly varying biases using a polynomial fit over a 1 hour duration, before evaluation of the standard deviation. Figure 6 shows an example of data from the 25th of May 2023, where an (almost) full day of clear sky was available. Over a two-hour period, the pointing precision is 56 µrad and 17 µrad for azimuth and elevation angles, respectively.

https://doi.org/10.5194/gi-2024-14
Preprint. Discussion started: 9 December 2024

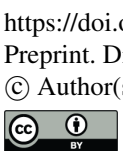

Geoscientific Instrumentation Methods and Data Systems Discussions

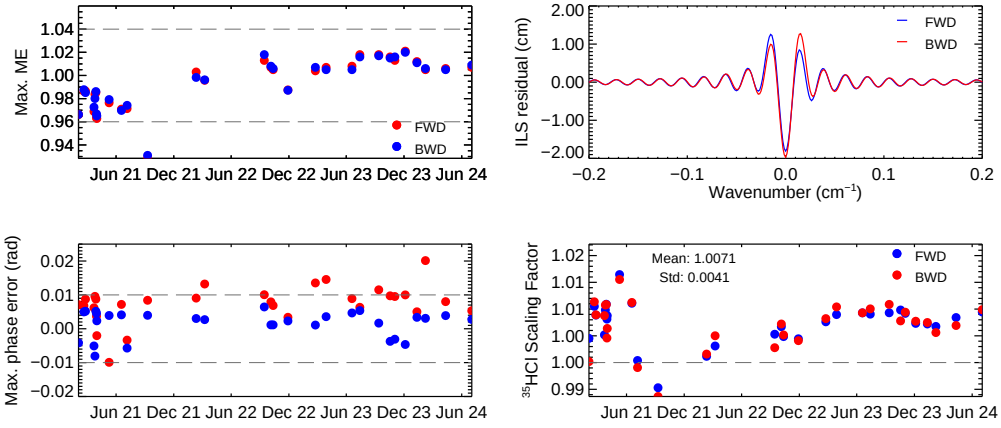

Figure 5. Extrema of the ME (a) and phase error (b) observed in each ILS measurement made over the last >3 years of operation. c) Corresponding $H^{35}Cl$ column normalized to the independently calibrated value. d) Example of residual between the ILS determined by LINEFIT and the theoretical ILS used in the retrieval processing software.

The presence of common absorbing species in both solar and Earth atmospheres allows an estimate of the accuracy to be made by observing the Doppler shift of the solar absorption line compared to the terrestrial. We follow the simple "single angle" approach described by (Gisi et al., 2011; Robinson et al., 2020) to estimate the pointing accuracy, rather than the full dual axis estimation reported by (Reichert et al., 2015). The relationship between θ, the angle subtended between the Sun centre and any point along the Sun equatorial axis, for an Earth observer, and the apparent solar line frequency ν is expressed by Eq. 2, in which R_s is the Sun radius, d is the Earth-Sun distance, v_T the equatorial tangential velocity of the heliosphere, ν_0 the terrestrial line frequency, and c the speed of light. The term in the $\arcsin$ function is always smaller than one per mil in all practical cases; therefore we can approximate $\arcsin(x) = x$, which leads to the expression of the pointing angular deviation θ as a linear function of the relative Doppler shift $\Delta\nu/\nu_0$.

https://doi.org/10.5194/gi-2024-14
Preprint. Discussion started: 9 December 2024

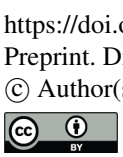

Geoscientific Instrumentation Methods and Data Systems Discussions

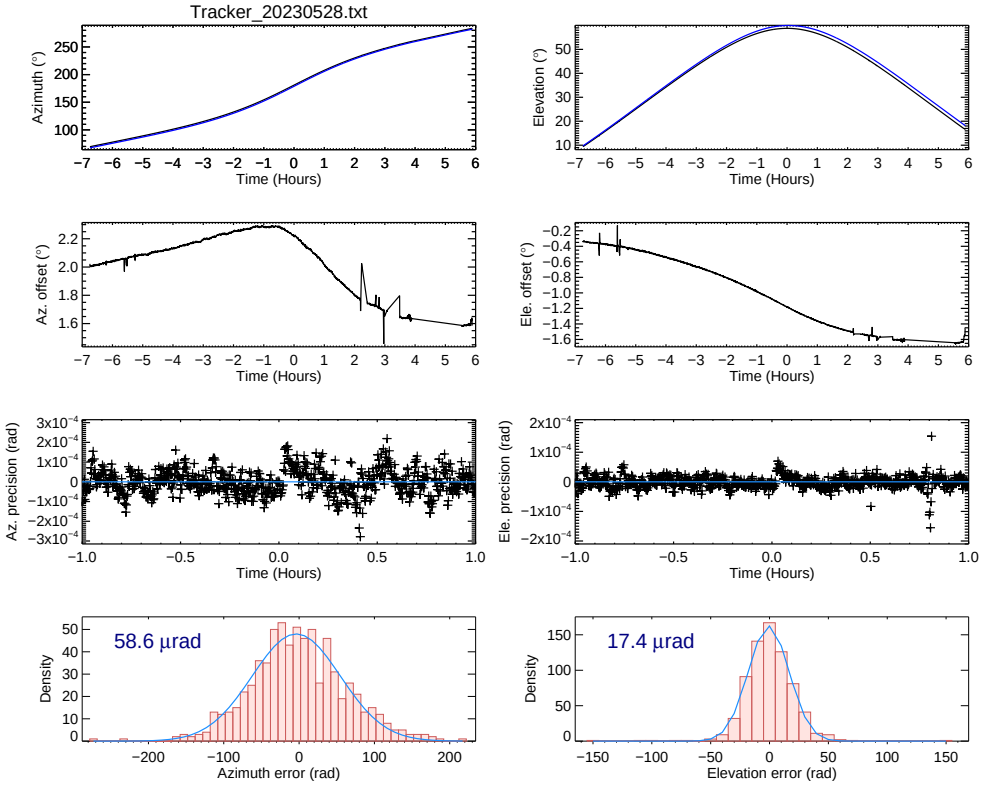

Figure 6. Estimation of the Sun tracker precision. The first (second) column corresponds to the azimuth (elevation) coordinate. From top to bottom, the plots represent 1) the actual and calculated angular coordinates of the Sun centre, 2) the residuals between actual and calculated angular coordinates, 3) the residuals further de-trended by a polynomial over a two hours period, 4) the histograms of the above with a fitted Gaussian distribution, whose standard deviation is given in the plot.

$$\theta = \arcsin\left[\frac{c \cdot R_s}{v_T \cdot d} \cdot \left(\frac{\nu}{\nu_0} - 1\right)\right] \approx \frac{c \cdot R_s}{v_T \cdot d} \cdot \frac{\Delta\nu}{\nu_0} \tag{2}$$

As part of the processing (to be described in the next section), the relative Doppler shift observed in the recorded spectra is determined from spectral fitting and can then be used as a estimator of pointing accuracy using Eq. 2. Figure 7 shows the estimated pointing accuracy as derived from Doppler shift, for nearly a year (2023).

4.4 Non linearity

The model used to process the data assumes linearity of the optical detectors. Any non-linearity between the photon flux received by the photodetectors of the FTS and the corresponding recorded signal can be identified by a distortion of the

https://doi.org/10.5194/gi-2024-14
Preprint. Discussion started: 9 December 2024

Geoscientific Instrumentation Methods and Data Systems Discussions

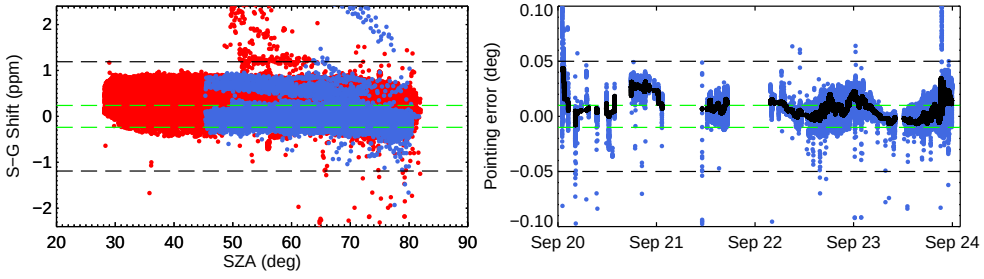

Figure 7. Estimation of the Sun tracker accuracy from solar line Doppler shift. Left: Solar gas shift (ppm) and Pointing error (deg) vs solar zenith angle (SZA). Blue = AM measurements, Red = PM measurements, Black dash = +/- 0.05 deg limit for max accepted error, Green dash = +/- 0.01 (ideal TCCON) limit for pointing error. Right: Pointing error time series for a year (Dec 2022 to end Nov 2023). Blue = pointing error, Black = 500 spectra rolling median, Dashed lines as previously.

low-pass filtered interferogram in the vicinity of the zero path difference (Abrams et al., 1994). This distortion exhibits a peak-like structure (Keppel-Aleks et al., 2007), from which a non-linearity metric is derived: the so called "dip" expressed as the amplitude of the distortion peak relative to the unmodulated interferogram amplitude. The non-linear distortion of the detector output relative to the photon flux to can either be saturation, and results in a negative dip, or an artifactual supralinearity, resulting in a positive dip (Corredera et al., 2003).

The dip metric, as derived by the processor, for the Harwell site is shown in Fig. 8. Considering the global mean of the dataset, the instrument appears to be affected by a slight non-linearity (superlinearity). However, individual estimates of dip are often outside the network norm (±0.5 per mil), with a large scatter that increases significantly with time, whist the probability distribution function remains Gaussian. The histogram plots in Fig. 8 are for subsets of 100 days taken in from 21/03/2021

https://doi.org/10.5194/gi-2024-14
Preprint. Discussion started: 9 December 2024


Geoscientific Instrumentation Methods and Data Systems Discussions

(clear histogram) and from 01/01/2024 and illustrate the widening of the scatter. The random nature of the dip metrics raises doubts whether it originates from true non-linearity in this case.

To investigate further in an independent manner, the 'out of band' regions of the InGaAs spectrum where no signal is expected were scrutinized. With detector non-linearity, the self-convolution of the spectrum produces a quadratic spectral artifact in the out-of-band regions between 0 and > 4000 cm^{-1}(Kleinert, 2006). Spectra were selected from dates between June 2021 and June 2024, taking in each case a spectrum from early morning, noon and late evening. Looking at the 3800-3900 cm^{-1} region for these spectra, no statistically significant offset was measured, indicating no non-linearity.

The dip parameter ought to be related to the power reaching the detector and to increase as the detector becomes more heavily saturated. By taking the unmodulated level of the interferograms as a proxy for optical power, no correlation with the dip amplitude was observed, for either detector channel.

Significant interference (at 50Hz and harmonics) can be seen in our interferograms. The source was confirmed as electrical in nature by varying the scanning velocity of the moving mirror of the interferometer. Using a tool developed by the Bremen site team (Buschmann, 2024), the actual dip, if any, can be visualized. Two cases are shown in the right hand side panel of Fig. 8 c) and d). Figure 8 c) shows a smoothed, DC corrected interferogram from 1st of June 2021, at 14:51 UTC. The vertical lines indicate the region around the ZPD in which the dip amplitude is determined and normalized to the unmodulated interferogram amplitude (blue line) to generate the dip parameter. The value for the case illustrated is 0.11 per mil. Figure 8 d) Shows similar trace for an interferogram from the 21st of March 2024 at 13:02 UTC. This suggests that the dip parameter is largely determined by the instantaneous properties of the electrical interference, and so is not a reliable indicator of non-linear detector behaviour. We are currently working to identify the source of the interference.

4.5 Laser sampling error

The spectrometer is fitted with the laser sampling board (LSB) developed for the TCCON. It allows optimization of the DC offset to the HeNe laser signal that provides the optical frequency reference to reduce the asymmetry in sampling interval, and hence reduces ghosting. Using a narrow-band filter at 6060 cm^{-1} to test the suppression, the ghost-parent suppression ratio was measured to be $\approx 5 \cdot 10^{-5}$. The laser sampling errors as outputted by the I2S software converting interferograms to spectra is Gaussian distributed with a mean of $-5 \cdot 10^{-6}$ and a standard deviation of $1.1 \cdot 10^{-4}$, expressed as fraction of sample step. This is well within the requirement of less than $2.4 \cdot 10^{-4}$.

5 Data Processing

5.1 Processing chain

The data processing chain has been implemented using the latest version (2020) of the GGG software (Laughner et al., 2023b). The level 1 data are timestamped transmission spectra of the atmosphere produced from the FTS interferograms and associated metadata. The I2S software (2020 release) performs the fast Fourier transform of single sided interferograms into spectra,

https://doi.org/10.5194/gi-2024-14
Preprint. Discussion started: 9 December 2024

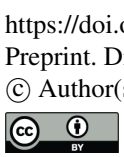

Geoscientific Instrumentation Methods and Data Systems Discussions
Open Access
EGU

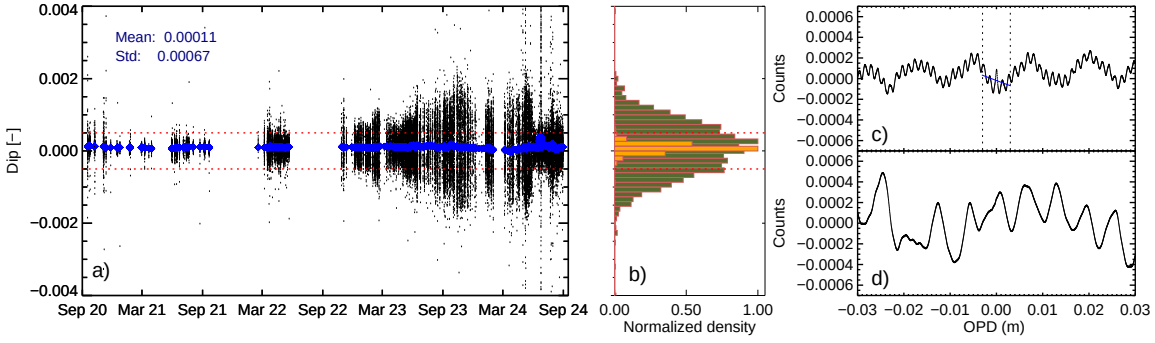

Figure 8. a) Evolution of the dip metric outputted by GGG over the whole Harwell site dataset. The blue points are a 1000 point smoothing, the red lines indicates the required norm to ensure insignificance of non linearity to the retrieved products. b) corresponding histogram of two data subset. The dark (light) histogram corresponds to January to April 2024 (March to June 2021). The right hand side panel shows smoothed, DC corrected interferograms. c) From 01/06/2021, the vertical lines indicate the ZPD area where the peak is searched, and the blue line the baseline correction for its normalization. d) From 21/03/2024. Both interferograms exhibits electrical noise pickup at mains frequency and harmonics.

https://doi.org/10.5194/gi-2024-14
Preprint. Discussion started: 9 December 2024


Geoscientific Instrumentation Methods and Data Systems Discussions

including removal of low frequency intensity fluctuations and Mertz phase correction. A script checks and only keeps the measurements where both channels are present and prepare the corresponding list for ingestion into GGG. Within the GGG software, a nonlinear least squared fitting of the level 1 data with an atmospheric transmission model is iteratively performed, by scaling the dry volume-mixing-ratio of atmospheric gases, until convergence between calculated and measured spectra is achieved and the residual is minimal, as seen in Fig. 9. The profiles are only scaled, the vertical distribution is determined from a priori data. The level 2 data produced are column-averaged dry VMR of gases X_{gas}.

The a priori gas VMR, pressure and temperature profiles originate from the near real time GEOS meteorological dataset referred as FP-IT (Forward Processing for Instrument Team), switched to GEOS-IT since 1 April 2024. For the TCCON, Caltech produces the extrapolated dataset relevant to each site, made available with a timeliness of 24 to 48 hours (Laughner et al., 2023a).

The processor uses correction factors for each retrieved species: one to account for mostly spectroscopy errors producing a bias on X_{gas} dependent on the solar zenith angle (air mass dependent correction factor ADCF) (Wunch et al., 2011), and one which is a global scaling (air mass independent scaling factor - AICF) designed to anchor the retrieved X_{gas} product to WMO-traceable in-situ measurements (Wunch et al., 2010). Currently, in absence of independent site calibration, the Harwell site processor uses the values that have been updated for the GGG2020 software release and are given in Laughner et al. (2023b). We are planning to attempt a site-specific update to the correction factors (Pollard et al., 2021) using the travelling standard methodology (Herkommer et al., 2024).

After the production of the level 2 data by GGG, the dataset is submitted (typically every quarter) for independent data quality assurance and control (QA/QC) by the network. Over the year 2023 for example, about 62% of the data submitted passed the QA/QC. The primary reason for flagging measurement of insufficient quality is cloud contamination.

Whilst using the standard GGG2020 retrieval, Harwell site specific "pre-processing" tasks have been implemented and are briefly described below.

5.1.1 Timing inconsistencies correction

During early data analysis, a systematic significant forward/backward scan bias in the X_{Luft} reported was observed (Brownsword et al., 2021). An inconsistency in the way the interferogram peak locations for forward and backward scans are stored in the Opus files for the two detector channels was found. It was confirmed that it arises from the version 2.485 of the Bruker IFS125 firmware (Pollard, 2021), also observed at the Lauder TCCON site (Pollard et al., 2017).

With this particular firmware, the parameter storing the peak location of the forward scan for the second (InGaAs) detector is incompatible with I2S, and produces a >10 s timestamp error. We followed the solution implemented by the Lauder team, and a python routine reconstructing the Opus file with the corrected interferogram peak locations was integrated to the processing chain.

https://doi.org/10.5194/gi-2024-14
Preprint. Discussion started: 9 December 2024

Geoscientific Instrumentation Methods and Data Systems Discussions
Open Access
EGU

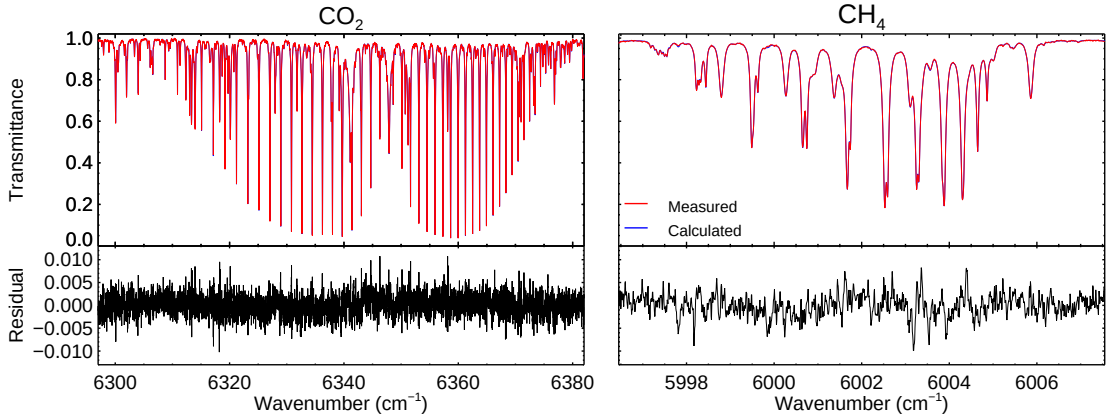

Figure 9. Examples of spectral fit and residual outcomes. Left, CO_2 micro-window centred at 6339 cm^{-1} from the 17th of July 2023, at 08:25 UTC. Right, CH_4 micro-window centred at 6002 cm^{-1} from the same record.

https://doi.org/10.5194/gi-2024-14
Preprint. Discussion started: 9 December 2024

Geoscientific Instrumentation Methods and Data Systems Discussions

5.1.2 In-situ meteorological data ingestion

Meteorological parameters are recorded independently of the TCCON measurements as described in Section 3.4 but on a synchronized time scale. Before starting the GGG processing, time series of temperature, pressure, and relative humidity are extracted and assigned to each forward-backward interferogram measurements. The zero path difference (ZPD) times of the forward and backward interferograms are calculated, and the meteorological data are interpolated with a spline fit at the central time between the two ZPD times, i.e., approximately 75 s after the forward interferogram ZPD. The two ZPD times differ about 150 s, the time it takes to record the two interferograms.

5.2 Dataset

The Harwell dataset covers about 4 years of operation at the time of writing (Weidmann et al., 2023). The record was started with a site manually operated during business hours, therefore limited in terms of data throughput. Between December 2021 and February 2022, the site was relocated to a different laboratory few 10's of meters away and did not operate. Between June 2022 and November 2022, a significant failure of the controller of the rotation stages, part of the Sun tracker, and subsequent long delivery time for a repair, prevented any measurements to take place. November 2022 onwards, system automation started to be deployed and a significant increase in data throughput is noticeable.

Figure 10 focuses on the X_{CO2} temporal series, and shows the associated seasonal variation model. The bottom panel of Fig. 10 shows the residual between the data and the model. The model developed by (Lindqvist et al., 2015) is used, and was fitted to the data using a Levenberg-Marquardt least-squares algorithm. The uncertainties on X_{CO2} derived from the GGG retrieval were fed into the fitting routine to propagate down to the seasonal cycle model parameters. The reduced χ^2 after fit convergence was 2.8, indicated a good input error scaling. The resulting model parameters and their uncertainties are given in Table 3.

Table 3. Fitted parameters of the Lindqvist model describing the Harwell X_{CO2} seasonal cycle.

a_o (ppm)	a_1 (ppm day^{-1})	a_2 (ppm)	a_3 (day)	a_4 (-)	a_5 (day)
413.36 ± 0.01	$(578 \pm 1)10^{-5}$	-3.242 ± 0.005	-7.90 ± 0.09	0.347 ± 0.003	-174.5 ± 0.4

The linear increase of X_{CO2} with time (coefficient a_1 in Table 3) is described by a gradient of 2.11 ppm/year. This is slightly less than the global 2.49 ppm/year rise averaged over 2021 - 2023 (Lan et al., 2024). The averaged seasonal cycle amplitude over the dataset ($2|a_2|$ from Table 3) is 6.48 ppm. For comparison to not-so-distant measurements at similar latitude, the amplitude appears lower than a typical temperate continental European TCCON site such as Bremen (53.1°N, 8.85°E) reported as 7.9 ppm (Jacobs et al., 2021), and higher than the 5.6 ppm (2000-2028 average) reported from in-situ measurements from Mace Head (53.3°N, 9.9°W) (Yun et al., 2022; Schuldt et al., 2023). The residual plot in Fig. 10 also shows that seasonal cycle amplitude is not constant over the four years of record. The mid-September 2023 trough is underestimated by the model.

https://doi.org/10.5194/gi-2024-14
Preprint. Discussion started: 9 December 2024

Geoscientific Instrumentation Methods and Data Systems Discussions
Open Access
EGU

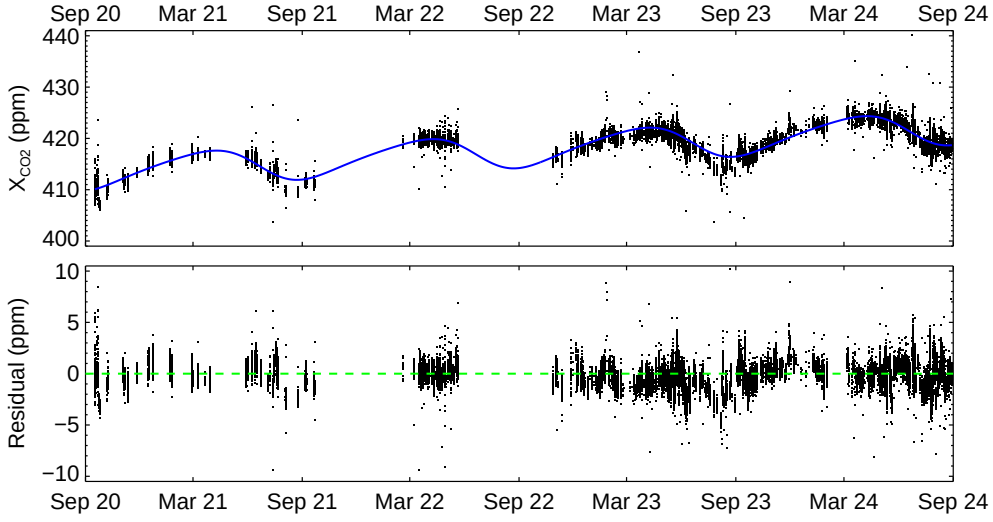

Figure 10. Harwell site X_{CO2} dataset (black dots). The temporal geophysical cycle was fitted to the model proposed by (Lindqvist et al., 2015), shown as a blue line. The lower panel provides the residual between the measured X_{CO2} and the modelled one.

Lastly, the seasonal cycle phasing can be described by the half drawdown day which is day 169 from the fitted model, well within the fairly scattered reported ensemble (Jacobs et al., 2021).

An excerpt of some other gas column VMR obtained from the Harwell site is shown in Fig. 11. The plot also shows (upper panel), the column averaged amount of dry air 'X_{luft}', which ideally should be equal to one, and therefore can be used as data quality diagnostic. The horizontal lines visualize the ±1% deviation from the ideal case. The vast majority of the data are well within the required interval.

For X_{CH4}, the annual trend is not constant: the annual rise over the years 2021 and 2023 is respectively 18.97 ±0.20 and 9.86 ±0.08 ppb/year, well within the global trends of 17.91 and 9.88 observed (Lan et al., 2024). The year 2022 was not calculated because only 3 month of data are available for 2022.

Within the dataset, some events are noticeable. In spring-summer 2023 plumes from the Canadian wildfires travelled over to Europe. Four distinct days in May and June 2023, the CO total column at Harwell increased by over 20 ppb compared to

https://doi.org/10.5194/gi-2024-14
Preprint. Discussion started: 9 December 2024

Geoscientific Instrumentation Methods and Data Systems Discussions

background days, producing spikes in the X_{CO} timeseries in Fig. 11. These events were corroborated using the near real time visualization tool from the Remote Sensing Group from RAL space (Latter et al., 2024), showing data derived from MetOp B and C with a Infrared-Microwave-Sounding retrieval scheme(Pope et al., 2021). Another similar event was observed again from the Canadian fires in August 2024.

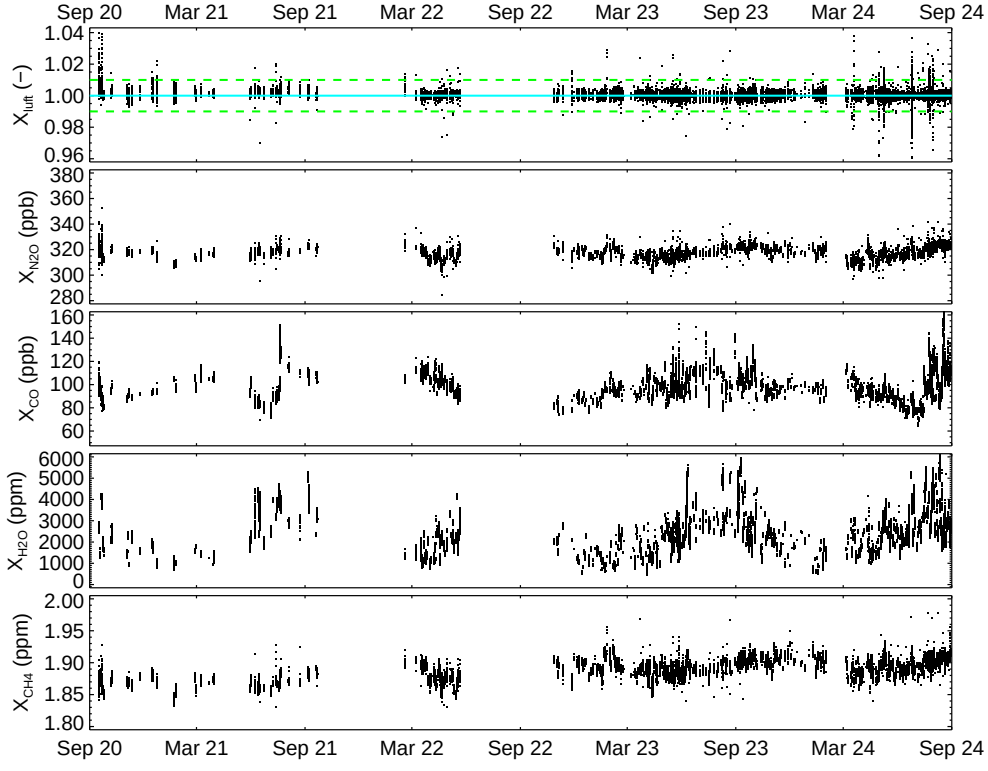

Figure 11. Harwell site column averaged dry mole fraction for the main molecules measured by the TCCON system.

6 Conclusions

The consistency and the data quality required across the global TCCON is essential to ensure the network fulfilled its demanding purposes of (i) greenhouse gas satellite data validation, (ii) linkage between *in-situ* and space-borne greenhouse gas measurements, and ultimately (iii) contributing to improving our knowledge of the carbon cycle. In this work, we transparently reported on the development and characterization of a new partnering observatory to demonstrate traceability of the Harwell site dataset quality down to the measurement system, and provide reference information about it.

https://doi.org/10.5194/gi-2024-14
Preprint. Discussion started: 9 December 2024


Geoscientific Instrumentation Methods and Data Systems Discussions
Open Access
EGU

The establishment of the Harwell TCCON observatory and its automation has been thoroughly described and its performance characterized, against the requirements agreed by the network, from instrumental parameters to data product quality metrics. The ad-hoc solar tracker system developed for the observatory was found to maintain the pointing accuracy very well. The particular firmware of the Fourier Transform Spectrometer used was found to suffer from a timing zero-path difference inconsistency. This has been corrected within the processing flow. Despite being free of non-linearity, the non-linearity 'dip' indicator was found to be affected by low frequency electrical pick-up noise (< 150Hz) producing artefactual non-linearity flagging.

The observatory has now produced a dataset spanning four years for averaged-column dry VMR of CO_2, CH_4, CO N_2O, H_2O, HDO, and HF, which have has been confirmed of required quality through the TCCON independent quality control process. The CO_2 seasonal cycle was characterized to be consistent with expectation for a northern mid-latitude location. CO spikes originating from plume transport from the Canadian forest fires we observed both in summer 2023 and 2024.

In the near term we are planning to further improve the site by: 1) installing a permanent alignment monitoring tool for the interferometer, 2) verifying the Harwell site consistency with some of the TCCON partners through the traveling standard methodology, and 3) improving on the data timeliness of the system.

Code availability. The code used to process the data presented in the paper is available from the TCCON community: https://github.com/TCCON/GGG

Data availability. As per the network standard, the Harwell data (Weidmann et al., 2023) comprising column-averaged dry volume mixing ratios of carbon dioxide (CO2), methane (CH4), nitrous oxide (N2O), hydrogen fluoride (HF), carbon monoxide (CO), water vapour (H2O), and deuterated water vapour (HDO) are available through the canonical repository for TCCON data (TCCON archive, 2024).

In addition, a mirror repository of the CalTech one has been set up for archival within the UK Centre for Environmental Data Analysis (CEDA TCCON archive, 2024). This ensures data collocation with the UK JASMIN computing facility. It also provides the meteorological data measured at the Harwell TCCON site.

Author contributions. DW: Harwell TCCON site principal investigator. Site installation, operation, and activities supervision. Manuscript preparation and writing. Data analysis. RB: Instrument and hardware facility setup. Instrument testing and characterization. Manuscript editing. SD: GGG2020 and software infrastructure implementation. Data processing.

Competing interests. No competing interests have been identified.

https://doi.org/10.5194/gi-2024-14
Preprint. Discussion started: 9 December 2024

Geoscientific Instrumentation Methods and Data Systems Discussions
Open Access
EGU

Acknowledgements. We gratefully acknowledge the TCCON community's constant readiness to support and share information. Rigel Kivi and Pauli Heikkinen have shared many hints from the Sodankylä site. Josh Laughner and Debra Wunch for help on GGG, Frank Hase for advice on Linefit, Dave Pollard and colleagues and Nick Deutscher regarding the forward-backward bias induced by the firmware bug. Matthias Buschmann on dip tools he developed. Kevin Smith, Andy Nave and Hilke Oetjen have also contributed to the very early stage of the Harwell facility establishment. James Powell is acknowledged for the development of the LabVIEW software control. Invaluable instrumental support was provided by Gregor Surawicz and colleagues at Bruker. We acknowledge financial support from RAL Space, the UK National Centre of Earth Observation (NCEO), and the UK National Environment Research Council (NERC).

https://doi.org/10.5194/gi-2024-14
Preprint. Discussion started: 9 December 2024

Geoscientific Instrumentation Methods and Data Systems Discussions

References

Abrams, M. C., Toon, G. C., and Schindler, R. A.: Practical example of the correction of Fourier-transform spectra for detector nonlinearity, Applied Optics, 33, 6307, https://doi.org/10.1364/AO.33.006307, 1994.

Babenhauserheide, A., Hase, F., and Morino, I.: Net CO2 fossil fuel emissions of Tokyo estimated directly from measurements of the Tsukuba TCCON site and radiosondes, Atmospheric Measurement Techniques, 13, 2697–2710, https://doi.org/10.5194/amt-13-2697-2020, 2020.

Brownsword, R., Doniki, S., and Weidmann, D.: Harwell TCCON Site accreditation application, https://doi.org/10.5281/zenodo.7950047, 2021.

Buschmann, M.: IFS125 preview, https://github.com/mbuschmann/ifs125preview, 2024.

Byrne, B., Liu, J., Bowman, K. W., Pascolini-Campbell, M., Chatterjee, A., Pandey, S., Miyazaki, K., van der Werf, G. R., Wunch, D., Wennberg, P. O., Roehl, C. M., and Sinha, S.: Carbon emissions from the 2023 Canadian wildfires, Nature, https://doi.org/10.1038/s41586-024-07878-z, 2024.

CEDA TCCON archive: Total Carbon Column Observing Network (TCCON), https://catalogue.ceda.ac.uk/uuid/3bfb7dfe4d354fb99864ae1d3de092c6/, 2024.

Corredera, P., Hernanz, M. L., Gonz lez-Herr ez, M., and Campos, J.: Anomalous non-linear behaviour of InGaAs photodiodes with overfilled illumination, Metrologia, 40, S150–S153, https://doi.org/10.1088/0026-1394/40/1/334, 2003.

Frey, M., Sha, M. K., Hase, F., Kiel, M., Blumenstock, T., Harig, R., Surawicz, G., Deutscher, N. M., Shiomi, K., Franklin, J. E., Bösch, H., Chen, J., Grutter, M., Ohyama, H., Sun, Y., Butz, A., Tsidu, G. M., Ene, D., Wunch, D., Cao, Z., Garcia, O., Ramonet, M., Vogel, F., and Orphal, J.: Building the COllaborative Carbon Column Observing Network (COCCON): long-term stability and ensemble performance of the EM27/SUN Fourier transform spectrometer, Atmospheric Measurement Techniques, 12, 1513–1530, https://doi.org/10.5194/amt-12-1513-2019, 2019.

Geddes, A., Robinson, J., and Smale, D.: Python-based dynamic scheduling assistant for atmospheric measurements by Bruker instruments using OPUS, Appl. Opt., 57, 689–691, https://doi.org/10.1364/AO.57.000689, 2018.

Geibel, M. C., Gerbig, C., and Feist, D. G.: A new fully automated FTIR system for total column measurements of greenhouse gases, Atmospheric Measurement Techniques, 3, 1363–1375, https://doi.org/10.5194/amt-3-1363-2010, 2010.

Gisi, M., Hase, F., Dohe, S., and Blumenstock, T.: Camtracker: a new camera controlled high precision solar tracker system for FTIR-spectrometers, Atmospheric Measurement Techniques, 4, 47–54, https://doi.org/10.5194/amt-4-47-2011, 2011.

Hase, F., Blumenstock, T., and Paton-Walsh, C.: Analysis of the instrumental line shape of high-resolution Fourier transform IR spectrometers with gas cell measurements and new retrieval software, Applied Optics, 38, 3417, https://doi.org/10.1364/AO.38.003417, 1999.

Hase, F., Drouin, B. J., Roehl, C. M., Toon, G. C., Wennberg, P. O., Wunch, D., Blumenstock, T., Desmet, F., Feist, D. G., Heikkinen, P., Mazière, M. D., Rettinger, M., Robinson, J., Schneider, M., Sherlock, V., Sussmann, R., Té, Y., Warneke, T., and Weinzierl, C.: Calibration of sealed HCl cells used for TCCON instrumental line shape monitoring, Atmospheric Measurement Techniques, 6, 3527–3537, https://doi.org/10.5194/amt-6-3527-2013, 2013.

Heikkinen, P. and Kivi, R.: Personal communication, 2020.

Herkommer, B., Alberti, C., Castracane, P., Chen, J., Dehn, A., Dietrich, F., Deutscher, N. M., Frey, M. M., Groß, J., Gillespie, L., Hase, F., Morino, I., Pak, N. M., Walker, B., and Wunch, D.: Using a portable FTIR spectrometer to evaluate the consistency of Total Carbon Column Observing Network (TCCON) measurements on a global scale: the Collaborative Carbon Column Observing Network (COCCON) travel standard, Atmospheric Measurement Techniques, 17, 3467–3494, https://doi.org/10.5194/amt-17-3467-2024, 2024.

https://doi.org/10.5194/gi-2024-14
Preprint. Discussion started: 9 December 2024

Geoscientific Instrumentation Methods and Data Systems Discussions

Jacobs, N., Simpson, W. R., Graham, K. A., Holmes, C., Hase, F., Blumenstock, T., Tu, Q., Frey, M., Dubey, M. K., Parker, H. A., Wunch, D., Kivi, R., Heikkinen, P., Notholt, J., Petri, C., and Warneke, T.: Spatial distributions of XCO2; seasonal cycle amplitude and phase over northern high-latitude regions, Atmospheric Chemistry and Physics, 21, 16 661–16 687, https://doi.org/10.5194/acp-21-16661-2021, 2021.

Keppel-Aleks, G., Toon, G. C., Wennberg, P. O., and Deutscher, N. M.: Reducing the impact of source brightness fluctuations on spectra obtained by Fourier-transform spectrometry, Applied Optics, 46, 4774, https://doi.org/10.1364/AO.46.004774, 2007.

Kivi, R. and Heikkinen, P.: Fourier transform spectrometer measurements of column CO2 at Sodankylä, Finland, Geoscientific Instrumentation, Methods and Data Systems, 5, 271–279, https://doi.org/10.5194/gi-5-271-2016, 2016.

Kleinert, A.: Correction of detector nonlinearity for the balloonborne Michelson Interferometer for Passive Atmospheric Sounding, Applied Optics, 45, 425, https://doi.org/10.1364/AO.45.000425, 2006.

Lan, X., Tans, P., and Thoning, K.: Trends in globally-averaged CO2 determined from NOAA Global Monitoring Laboratory measurements, https://doi.org/10.15138/9N0H-ZH07, 2024.

Latter, B., Siddans, R., Thomas, G., and Kerridge, B.: RAL Space Remote Rensing Group data vizualization portal, http://rsg.rl.ac.uk/vistool/?cal=2023-05-28&proj=nimsmc+nimsmb&vars=c04d1dcbp+c04d1dcbp&rloc=46.08C3.02C-2052.08C8385425.43&lch=1+1, accessed: 2024-10-16, 2024.

Laughner, J. L., Roche, S., Kiel, M., Toon, G. C., Wunch, D., Baier, B. C., Biraud, S., Chen, H., Kivi, R., Laemmel, T., McKain, K., Quéhé, P.-Y., Rousogenous, C., Stephens, B. B., Walker, K., and Wennberg, P. O.: A new algorithm to generate a priori trace gas profiles for the GGG2020 retrieval algorithm, Atmospheric Measurement Techniques, 16, 1121–1146, https://doi.org/10.5194/amt-16-1121-2023, 2023a.

Laughner, J. L., Toon, G. C., Mendonca, J., Petri, C., Roche, S., Wunch, D., Blavier, J.-F., Griffith, D. W. T., Heikkinen, P., Keeling, R. F., Kiel, M., Kivi, R., Roehl, C. M., Stephens, B. B., Baier, B. C., Chen, H., Choi, Y., Deutscher, N. M., Digangi, J. P., Gross, J., Herkommer, B., Jeseck, P., Laemmel, T., Lan, X., Mcgee, E., Mckain, K., Miller, J., Morino, I., Notholt, J., Ohyama, H., Pollard, D. F., Rettinger, M., Riris, H., Rousogenous, C., Kumar, M., 25, S., Shiomi, K., Strong, K., Sussmann, R., Té, Y., Velazco, V. A., Wofsy, S. C., Zhou, M., Wennberg, P. O., Paulson, J. A., and Laughner, J.: The Total Carbon Column Observing Network's GGG2020 Data Version, Earth Syst. Sci. Data Discuss., p. 20771, https://doi.org/10.5194/essd-2023-331, 2023b.

Lindqvist, H., O'Dell, C. W., Basu, S., Boesch, H., Chevallier, F., Deutscher, N., Feng, L., Fisher, B., Hase, F., Inoue, M., Kivi, R., Morino, I., Palmer, P. I., Parker, R., Schneider, M., Sussmann, R., and Yoshida, Y.: Does GOSAT capture the true seasonal cycle of carbon dioxide?, Atmospheric Chemistry and Physics, 15, 13 023–13 040, https://doi.org/10.5194/acp-15-13023-2015, 2015.

Messerschmidt, J., Parazoo, N., Wunch, D., Deutscher, N. M., Roehl, C., Warneke, T., and Wennberg, P. O.: Evaluation of seasonal atmosphere–biosphere exchange estimations with TCCON measurements, Atmospheric Chemistry and Physics, 13, 5103–5115, https://doi.org/10.5194/acp-13-5103-2013, 2013.

Michalsky, J. J.: The Astronomical Almanac's algorithm for approximate solar position (1950–2050), Solar Energy, 40, 227–235, https://doi.org/10.1016/0038-092X(88)90045-X, 1988.

Mottungan, K., Brocchi, V., Roychoudhury, C., Gaubert, B., Tang, W., Mirrezaei, M. A., McKinnon, J., Guo, Y., and Arellano, A.: Local and Regional Enhancements of CH4, CO, and CO2 Inferred from TCCON Column Measurements, EGUsphere, 2024, 1–45, https://doi.org/10.5194/egusphere-2024-705, 2024.

Pollard, D.: Personal communication, 2021.

Pollard, D. F., Sherlock, V., Robinson, J., Deutscher, N. M., Connor, B., and Shiona, H.: The Total Carbon Column Observing Network site description for Lauder, New Zealand, Earth System Science Data, 9, 977–992, https://doi.org/10.5194/essd-9-977-2017, 2017.

https://doi.org/10.5194/gi-2024-14
Preprint. Discussion started: 9 December 2024

Geoscientific Instrumentation Methods and Data Systems Discussions

Pollard, D. F., Robinson, J., Shiona, H., and Smale, D.: Intercomparison of Total Carbon Column Observing Network (TCCON) data from two Fourier transform spectrometers at Lauder, New Zealand, Atmospheric Measurement Techniques, 14, 1501–1510, https://doi.org/10.5194/amt-14-1501-2021, 2021.

Pope, R. J., Kerridge, B. J., Siddans, R., Latter, B. G., Chipperfield, M. P., Arnold, S. R., Ventress, L. J., Pimlott, M. A., Graham, A. M., Knappett, D. S., and Rigby, R.: Large Enhancements in Southern Hemisphere Satellite-Observed Trace Gases Due to the 2019/2020 Australian Wildfires, Journal of Geophysical Research: Atmospheres, 126, https://doi.org/10.1029/2021JD034892, 2021.

Reichert, A., Hausmann, P., and Sussmann, R.: Pointing errors in solar absorption spectrometry – correction scheme and its validation, Atmospheric Measurement Techniques, 8, 3715–3728, https://doi.org/10.5194/amt-8-3715-2015, 2015.

Robinson, J., Smale, D., Pollard, D., and Shiona, H.: Solar tracker with optical feedback and continuous rotation, Atmospheric Measurement Techniques, 13, 5855–5871, https://doi.org/10.5194/amt-13-5855-2020, 2020.

Schuldt, K. N., Mund, J., Aalto, T., Abshire, J. B., Aikin, K., Allen, G., Arlyn Andrews, Apadula, F., Arnold, S., Baier, B., Bakwin, P., Bäni, L., Bartyzel, J., Bentz, G., Bergamaschi, P., Beyersdorf, A., Biermann, T., Biraud, S. C., Pierre-Eric Blanc, Boenisch, H., Bowling, D., Brailsford, G., Brand, W. A., Brunner, D., Bui, T. P. V., Van Den Bulk, P., Francescopiero Calzolari, Chang, C. S., Chen, G., Huilin Chen, Lukasz Chmura, St. Clair, J. M., Clark, S., Sites Climadat, Coletta, J. D., Colomb, A., Commane, R., Condori, L., Conen, F., Conil, S., Couret, C., Cristofanelli, P., Cuevas, E., Curcoll, R., Daube, B., Davis, K. J., Dean-Day, J. M., Delmotte, M., Dickerson, R., DiGangi, E., DiGangi, J. P., Van Dinther, D., Elkins, J. W., Elsasser, M., Emmenegger, L., Shuangxi Fang, Fischer, M. L., Forster, G., France, J., Frumau, A., Fuente-Lastra, M., Galkowski, M., Gatti, L. V., Gehrlein, T., Gerbig, C., Francois Gheusi, Gloor, E., Goto, D., Griffis, T., Hammer, S., Hanisco, T. F., Hanson, C., Haszpra, L., Hatakka, J., Heimann, M., Heliasz, M., Heltai, D., Henne, S., Hensen, A., Hermans, C., Hermansen, O., Hintsa, E., Hoheisel, A., Holst, J., Di Iorio, T., Iraci, L. T., Ivakhov, V., Jaffe, D. A., Jordan, A., Joubert, W., Kang, H.-Y., Karion, A., Kawa, S. R., Kazan, V., Keeling, R. F., Keronen, P., Jooil Kim, Klausen, J., Kneuer, T., Ko, M.-Y., Kolari, P., Kominkova, K., Kort, E., Kozlova, E., Krummel, P. B., Kubistin, D., Kulawik, S. S., Kumps, N., Labuschagne, C., Lam, D. H., Lan, X., Langenfelds, R. L., Lanza, A., Laurent, O., Laurila, T., Lauvaux, T., Lavric, J., Law, B. E., Choong-Hoon Lee, Haeyoung Lee, Lee, J., Lehner, I., Lehtinen, K., Leppert, R., Leskinen, A., Leuenberger, M., W.H. Leung, Levin, I., Levula, J., Lin, J., Lindauer, M., Lindroth, A., Mikaell Ottosson Löfvenius, Loh, Z. M., Lopez, M., Lunder, C. R., Machida, T., Mammarella, I., Manca, G., Manning, A., Manning, A., Marek, M. V., Marklund, P., Marrero, J. E., Martin, D., Martin, M. Y., Giordane A. Martins, Matsueda, H., De Mazière, M., McKain, K., Meijer, H., Meinhardt, F., Merchant, L., Jean-Marc Metzger, N. Mihalopoulos, Miles, N. L., Miller, C. E., Miller, J. B., Mitchell, L., Mölder, M., Monteiro, V., Montzka, S., Moore, F., Moossen, H., Morgan, E., Josep-Anton Morgui, Morimoto, S., Müller-Williams, J., J. William Munger, Munro, D., Mutuku, M., Myhre, C. L., Shin-Ichiro Nakaoka, Jaroslaw Necki, Newman, S., Nichol, S., Nisbet, E., Niwa, Y., Njiru, D. M., Noe, S. M., Nojiri, Y., O'Doherty, S., Obersteiner, F., Paplawsky, B., Parworth, C. L., Peischl, J., Peltola, O., Peters, W., Philippon, C., Piacentino, S., Pichon, J. M., Pickers, P., Piper, S., Pitt, J., Plass-Dülmer, C., Platt, S. M., Prinzivalli, S., Ramonet, M., Ramos, R., Xinrong Ren, Reyes-Sanchez, E., Richardson, S. J., Louis-Jeremy Rigouleau, Riris, H., Rivas, P. P., Rothe, M., Yves-Alain Roulet, Ryerson, T., Ju-Mee Ryoo, Sargent, M., Di Sarra, A. G., Sasakawa, M., Scheeren, B., Schmidt, M., Schuck, T., Schumacher, M., Seibel, J., Seifert, T., Sha, M. K., Shepson, P., Shook, M., Sloop, C. D., Smith, P. D., Sørensen, L. L., De Souza, R. A. F., Spain, G., Steger, D., Steinbacher, M., Stephens, B., Sweeney, C., Taipale, R., Takatsuji, S., Tans, P., Thoning, K., Timas, H., Torn, M., Trisolino, P., Turnbull, J., Vermeulen, A., Viner, B., Vitkova, G., Walker, S., Watson, A., Weiss, R., De Wekker, S., Weyrauch, D., Wofsy, S. C., Worsey, J., Worthy, D., Xueref-Remy, I., Yates, E. L., Dickon Young, Yver-Kwok, C., Zaehle, S., Zahn, A., Zellweger, C., and Miroslaw Zimnoch: Multi-laboratory compilation of atmospheric carbon dioxide data for the period 1957-2022, https://doi.org/10.25925/20231201, 2023.

Sha, M. K., Mazière, M. D., Notholt, J., Blumenstock, T., Chen, H., Dehn, A., Griffith, D. W. T., Hase, F., Heikkinen, P., Hermans, C., Hoffmann, A., Huebner, M., Jones, N., Kivi, R., Langerock, B., Petri, C., Scolas, F., Tu, Q., and Weidmann, D.: Intercomparison of low- and high-resolution infrared spectrometers for ground-based solar remote sensing measurements of total column concentrations of CO2, CH4, and CO, Atmospheric Measurement Techniques, 13, 4791–4839, https://doi.org/10.5194/amt-13-4791-2020, 2020.

Sha, M. K., Langerock, B., Blavier, J.-F. L., Blumenstock, T., Borsdorff, T., Buschmann, M., Dehn, A., Mazière, M. D., Deutscher, N. M., Feist, D. G., García, O. E., Griffith, D. W. T., Grutter, M., Hannigan, J. W., Hase, F., Heikkinen, P., Hermans, C., Iraci, L. T., Jeseck, P., Jones, N., Kivi, R., Kumps, N., Landgraf, J., Lorente, A., Mahieu, E., Makarova, M. V., Mellqvist, J., Metzger, J.-M., Morino, I., Nagahama, T., Notholt, J., Ohyama, H., Ortega, I., Palm, M., Petri, C., Pollard, D. F., Rettinger, M., Robinson, J., Roche, S., Roehl, C. M., Röhling, A. N., Rousogenous, C., Schneider, M., Shiomi, K., Smale, D., Stremme, W., Strong, K., Sussmann, R., Té, Y., Uchino, O., Velazco, V. A., Vigouroux, C., Vrekoussis, M., Wang, P., Warneke, T., Wizenberg, T., Wunch, D., Yamanouchi, S., Yang, Y., and Zhou, M.: Validation of methane and carbon monoxide from Sentinel-5 Precursor using TCCON and NDACC-IRWG stations, Atmospheric Measurement Techniques, 14, 6249–6304, https://doi.org/10.5194/amt-14-6249-2021, 2021.

Taylor, T. E., O'Dell, C. W., Crisp, D., Kuze, A., Lindqvist, H., Wennberg, P. O., Chatterjee, A., Gunson, M., Eldering, A., Fisher, B., Kiel, M., Nelson, R. R., Merrelli, A., Osterman, G., Chevallier, F., Palmer, P. I., Feng, L., Deutscher, N. M., Dubey, M. K., Feist, D. G., García, O. E., Griffith, D. W. T., Hase, F., Iraci, L. T., Kivi, R., Liu, C., Mazière, M. D., Morino, I., Notholt, J., Oh, Y.-S., Ohyama, H., Pollard, D. F., Rettinger, M., Schneider, M., Roehl, C. M., Sha, M. K., Shiomi, K., Strong, K., Sussmann, R., Té, Y., Velazco, V. A., Vrekoussis, M., Warneke, T., and Wunch, D.: An 11-year record of XCO2 estimates derived from GOSAT measurements using the NASA ACOS version 9 retrieval algorithm, Earth System Science Data, 14, 325–360, https://doi.org/10.5194/essd-14-325-2022, 2022.

TCCON archive: Total Carbon Column Observing Network (TCCON), https://tccondata.org/, 2024.

Toon, G. C.: Timing Information in OPUS files - Calculation of ZPD time, https://tccon-wiki.caltech.edu/pub/Main/TechnicalDocuments/opus_zpd_time_20090326.pdf, accessed: 2024-01-04, 2009.

Treffers, R. R.: Signal-to-noise ratio in Fourier spectroscopy, Applied Optics, 16, 3103, https://doi.org/10.1364/AO.16.003103, 1977.

UK Met Office: Air masses and weather fronts, National Meteorological Library and Archive, 2018.

Walraven, R.: Calculating the position of the sun, Solar Energy, 20, 393–397, https://doi.org/https://doi.org/10.1016/0038-092X(78)90155-X, 1978.

Weidmann, D., Brownsword, R., and Doniki, S.: TCCON data from Harwell, Oxfordshire (UK), Release GGG2020.R0, https://doi.org/10.14291/tccon.ggg2020.harwell01.R0, funding by Science and Technology Facilities Council GRID grid.14467.30., 2023.

Wunch, D., Toon, G. C., Wennberg, P. O., Wofsy, S. C., Stephens, B. B., Fischer, M. L., Uchino, O., Abshire, J. B., Bernath, P., Biraud, S. C., Blavier, J.-F. L., Boone, C., Bowman, K. P., Browell, E. V., Campos, T., Connor, B. J., Daube, B. C., Deutscher, N. M., Diao, M., Elkins, J. W., Gerbig, C., Gottlieb, E., Griffith, D. W. T., Hurst, D. F., Jiménez, R., Keppel-Aleks, G., Kort, E. A., Macatangay, R., Machida, T., Matsueda, H., Moore, F., Morino, I., Park, S., Robinson, J., Roehl, C. M., Sawa, Y., Sherlock, V., Sweeney, C., Tanaka, T., and Zondlo, M. A.: Calibration of the Total Carbon Column Observing Network using aircraft profile data, Atmospheric Measurement Techniques, 3, 1351–1362, https://doi.org/10.5194/amt-3-1351-2010, 2010.

Wunch, D., Toon, G. C., Blavier, J.-F. L., Washenfelder, R. A., Notholt, J., Connor, B. J., Griffith, D. W. T., Sherlock, V., and Wennberg, P. O.: The Total Carbon Column Observing Network, Philosophical Transactions of the Royal Society A: Mathematical, Physical and Engineering Sciences, 369, 2087–2112, https://doi.org/10.1098/rsta.2010.0240, 2011.

Wunch, D., Wennberg, P. O., Osterman, G., Fisher, B., Naylor, B., Roehl, C. M., O'Dell, C., Mandrake, L., Viatte, C., Kiel, M., Griffith, D. W. T., Deutscher, N. M., Velazco, V. A., Notholt, J., Warneke, T., Petri, C., Maziere, M. D., Sha, M. K., Sussmann, R., Rettinger, M.,

https://doi.org/10.5194/gi-2024-14
Preprint. Discussion started: 9 December 2024

Geoscientific Instrumentation Methods and Data Systems Discussions
Open Access
EGU

Pollard, D., Robinson, J., Morino, I., Uchino, O., Hase, F., Blumenstock, T., Feist, D. G., Arnold, S. G., Strong, K., Mendonca, J., Kivi, R., Heikkinen, P., Iraci, L., Podolske, J., Hillyard, P. W., Kawakami, S., Dubey, M. K., Parker, H. A., Sepulveda, E., García, O. E., Te, Y., Jeseck, P., Gunson, M. R., Crisp, D., and Eldering, A.: Comparisons of the Orbiting Carbon Observatory-2 (OCO-2) XCO2 measurements with TCCON, Atmospheric Measurement Techniques, 10, 2209–2238, https://doi.org/10.5194/amt-10-2209-2017, 2017.

Yang, D., Boesch, H., Liu, Y., Somkuti, P., Cai, Z., Chen, X., Noia, A. D., Lin, C., Lu, N., Lyu, D., Parker, R. J., Tian, L., Wang, M., Webb, A., Yao, L., Yin, Z., Zheng, Y., Deutscher, N. M., Griffith, D. W. T., Hase, F., Kivi, R., Morino, I., Notholt, J., Ohyama, H., Pollard, D. F., Shiomi, K., Sussmann, R., Té, Y., Velazco, V. A., Warneke, T., and Wunch, D.: Toward High Precision XCO 2 Retrievals From TanSat Observations: Retrieval Improvement and Validation Against TCCON Measurements, Journal of Geophysical Research: Atmospheres, 125, https://doi.org/10.1029/2020JD032794, 2020.

Yun, J., Jeong, S., Gruber, N., Gregor, L., Ho, C.-H., Piao, S., Ciais, P., Schimel, D., and Kwon, E. Y.: Enhance seasonal amplitude of atmospheric CO2 by the changing Southern Ocean carbon sink, Science Advances, 8, https://doi.org/10.1126/sciadv.abq0220, 2022.